GT2023-102667

OPERATIONAL STRATEGIES OF 2-SPOOL MICRO GAS TURBINE WITH ALTERNATIVE FUELS: A PERFORMANCE ASSESSMENT

Aggelos Gaitanis*
Université Catholique de Louvain,
University of Mons (UMONS)
Belgium

Ravi Nath Tiwari
Thermochemical Power Group (TPG)
University of Genoa
Italy

Ward De Paepe
Thermal Engineering and
Combustion Research Unit
University of Mons (UMONS)
Belgium

Mario Luigi Ferrari
Thermochemical Power Group (TPG)
University of Genoa
Italy

Francesco Contino
Thermodynamics and
fluid mechanics (TFL)
Université Catholique de Louvain
Belgium

Peter Breuhaus
NORCE
Norwegian Research Centre AS
Norway

ABSTRACT

The demand for efficient, cost-effective, and low-emission decentralized electricity and heat production is rapidly increasing. Micro Gas Turbines (mGT) have not yet succeeded in conquering the small-scale combined heat and power (CHP) market. The main reason is that their electrical efficiency is not high enough to maintain a cost-effective operation at low heat demand. A two-shaft intercooled mGT has the potential to meet the current market demand for decentralized power generation. This technology maintains a high level of electrical efficiency even at part load and coupled with its fuel-flexible combustion chamber, makes it an ideal candidate for CHP concepts in a renewable future.

The energy transition however also requires mGTs to be able to run on alternative fuels, such as hydrogen and syngas, which shifts its operating conditions and requires significant modification in the cycle's part-load control to ensure the stable operation of the components such as the compressor. Therefore, in this paper, performance analysis on a 2-spool mGT is carried out using a mixture of natural gas, syngas, and hydrogen as a fuel. Specific attention is given to the low-pressure and high-pressure compressors and the variation of surge margin by adding hydrogen and syngas into the fuel. Two control strategies of the 2-spool mGT are adopted. In the first scenario, the two shafts have the same rotational speed while in the second one, the shaft speeds are controlled independently. In both part-load strategies, the specific performance of the two compressors keeps high isentropic efficiency which leads to high electrical efficiency at nominal power when natural gas–syngas mixture is used as fuel. When the engine is operated with equal shaft speeds, the maximum performance with 100 vol.% of syngas is observed at 85% of the nominal load while 100 vol.% of hydrogen shows maximum efficiency at an electric load of 63.7%. Also, at electric power lower than 60% of the nominal and for high amounts of syngas in natural gas, the low-pressure compressor (LPC) operates closely to surge line. In the second part-load strategy, the efficiency increases as the load decreases and the LPC runs in an efficient and safe operating region. Moreover, the performance of the 2-spool mGT is significantly influenced by the amount of nitrogen in syngas. At 200 kW, 45 vol.% of nitrogen decreases the airflow rate of the cycle by 7.4 % compared to 0 vol.%. The results indicate that the amount of nitrogen in syngas and also the part-load strategies significantly influence the safe operation of the LPC component.

Keywords: microturbine, 2-spool machine, numerical, steady-state, part-load, hydrogen, syngas

NOMENCLATURE
Acronyms

CC	combustion chamber
CFD	computational fluid dynamics
CHP	combined heat and power

*Address all correspondence to this author. Tel: +32 10 47 22 00,
Email: angelos.gaitanis@uclouvian.be

FAR	fuel to air ratio [-]	
HPC	high-pressure compressor	
HPT	high-pressure turbine	
ICE	internal combustion engine	
LHV	lower heating value [MJ/kg]	
LPC	low-pressure compressor	
LPT	low-pressure turbine	
mGT	micro gas turbine	
mHAT	micro humid air turbine	
NG	natural gas	
ORC	organic rankine cycle	
PR	pressure ratio [-]	
SG	synthesis gas (syngas)	
STIG	steam-injected gas turbine	
TIT	turbine inlet temperature [ºC]	
TET	turbine exhaust temperature [ºC]	

Roman symbol

C_p	constant pressure heat capacity	kJ/(kgK)
h	specific enthalpy	J/kg
K_c	choke constant	-
$\dot{m}$	mass flow rate	kg/s
N	rotational speed	rpm
P	power	kW
p	pressure	Pa
T	temperature	ºC

Greek symbols

η	efficiency	%
π	pressure ratio	-
ε	heat exchanger effectiveness	-

subscripts

air	properties of air
des	design value
el	electrical
fuel	properties of fuel
int	intercooler
rec	recuperator
red	reduced

INTRODUCTION

Renewable energy systems are being discussed globally, which has led to an increase in the use of low-emission energy resources. If low-emission technologies and renewable fuels are not introduced promptly and the electricity production will continue to grow rapidly, a significant increase in greenhouse gas emissions will be observed in the coming decades. Decentralized and hybrid power systems present many benefits (i.e., improving overall efficiency and minimizing emissions) [3] in future power production. In that context, micro gas turbines (mGT) could play an important role in such systems, but their low efficiency and high specific price per kilowatt prevent them from being implemented effectively. Micro gas turbines power capacities are not well defined but are generally specified between 10 kW and 500 kW [4]. The typical performance of such an engine is lower than that of their competitor in the market (i.e., internal combustion engines - ICE).

Historically, microturbine technology has been researched since 1970, when the automotive industry began to consider replacing reciprocating piston engines [4][5]. Microturbines have not had great success in the automotive sector as they show lower transient response and higher cost compared to ICE [4]. However, they could play an imperative role in developing decentralized and hybrid energy systems in the current era. By increasing their performance coupled with state-of-the-art technologies and using renewable fuels, they could meet market demand in terms of emissions and efficiency.

Micro gas turbines are considered to be promising technologies due to their fuel flexibility, low emissions, high power density, and low maintenance costs [6][7]. Despite their relatively low exhaust temperatures (around 150–300ºC), their waste heat can still be utilized to generate low-pressure steam and/or hot water [4]. The heat provided in mGT exhaust allows it to be implemented in combined cycle concepts [8]. The thermal recovery performed by the organic Rankine cycle (ORC) bottomed to an mGT can increase the combined cycle thermal efficiency by 15% [9]. Also, concepts like the micro humid air turbine (mHAT) [10] proved to increase the performance of the engine significantly. Moreover, bladeless or Tesla technology can play a vital role in increasing the compressor performance due to its reversible operation, low manufacturing costs and low noise [11]. In that context, an alternative mGT concept, which is the two-spool intercooled mGT, was introduced. This engine seems capable of successfully conquering the small-scale CHP market. This 2-spool intercooled mGT presents an electrical efficiency of around 40% and is capable to incorporate a range of fuels [12]. In literature, two studies can be found that described the design of this engine [13,14], where especially Malkamäki et al. have indicated that its efficiency and cost can be compared with a reciprocating engine from MWM company of the same load [13].

Besides increasing the efficiency of decentralized production, the world also focuses on renewable fuels, such as hydrogen, syngas, and biogas [3,15], in response to the growing demand for low-emission technologies. The shift towards more renewable energy production also pushes the mGT to become more flexible in terms of fuel utilization. Therefore, apart from natural gas, alternative fuels with lower energy content like syngas and biogas should be used. Moreover, the energy transition requires the utilization of hydrogen as a main fuel. Given the occasionally limited availability of these fuels, the mGT should thus be capable of running on both classical fossil-based gaseous fuels, hydrogen which has a high lower heating value (LHV) and alternative fuels like syngas with a rather low LHV. The addition of alternative fuels could restrict the

mGT operation as compressor surge can occur due to the decreasing air mass flow rate. Also, the combustion process when natural gas is mixed with syngas or hydrogen can cause combustion instabilities, leading to flameout (syngas) or flashback (hydrogen).

Having that in mind, researchers [16–19] studied the impact of using hydrogen and/or a blend of natural gas/hydrogen on the mGT both numerically and experimentally. Hydrogen addition in methane increased the flame temperatures with the cooling and NOx emissions being the primary concerns [16,17]. Also, an experimental and numerical study on pure hydrogen-fueled gas turbine highlighted the higher outlet velocity and pressure drop in the combustion chamber (CC) compared to pure natural gas operation [18]. Pappa et al. showed that the reactivity of hydrogen can be lower by applying steam as a diluent using large eddy simulation [19].

Similarly, different combustion challenges are observed when syngas is used instead of hydrogen. Bompas et al. [17] numerically compared carbon monoxide levels when using natural gas or syngas indicating that the use of syngas does not significantly impact combustion efficiency. Diaz et al. [21] examined the energy and exergy efficiencies of a syngas mGT cogeneration system, while also analyzing the total costs associated with the production of energy from syngas obtained by gasification. They showed that increasing the compression ratio improves the thermodynamic performance, but the cost of the system per unit of time is increased as well. Furthermore, it was found that the CC presented the highest rate of exergy destruction [21]. Thermodynamic and computational fluid dynamics (CFD) analyses have been performed on a small-scale integrated energy system composed of mGT-ORC-gasifier focusing on the performances of five different syngas-biogas fuels. This study indicated the necessity of operating the mGT in particular conditions, determined by the compressor and turbine performance maps of the AE-T100 due to the low LHV of the fuels [22]. Renzi et al. assessed numerically the behavior of the same mGT cycle when it is fed with biomass-derived syngas showing that the use of syngas decreased the overall efficiency of the system by 5% due to the higher thermal input that is required to keep the produced power at the nominal value [23]. They also included a steam injection gas turbine (STIG) cycle to counteract the negative effects of syngas utilization on the cycle performance. De Paepe et al. extended the work of Renzi et al. by comparing two steady-state models and validating them in their capability to simulate steam injection in the T100 mGT fed with natural gas and syngas [24]. When the cycle runs with syngas some variation in performance parameters between both models is observed which confirms the importance of the accurate and extensive modeling of the combustion chamber [24].

The above-mentioned studies analyze the performance characteristics of running mGT engines with alternative fuels. Numerical and experimental works studied the exhaust gas emissions and the required design modifications of CC to incorporate syngas or hydrogen. Although, extensive performance analysis on one of the most promising mGT (i.e., 2-spool mGT) in the market, by utilizing several alternative fuel mixtures, is still missing in the literature. The purpose of this article is thus to study the performance of a 2-spool mGT from a thermodynamic point of view when applying various fuel mixtures including natural gas (NG), syngas (SG), and hydrogen (H_2). For this analysis, a steady-state model of the 2-spool engine was developed in Python programming language and the combustion mechanisms were embedded according to GRI-Mech 3.0 library. As validation, the 0-D model is compared with another model of the 2-spool mGT from the literature. Additionally, two part-load strategies are employed for the steady-state modeling of this cycle to simulate the part-load behavior. These strategies are compared regarding the produced electrical efficiency (η_{el}) and the behavior of both compressors.

The structure of this paper is as follows: In the Methodology section, the numerical model is described thoroughly and the two part-load strategies regarding the operation of the cycle are presented. In the Results section, the behavior of several fuel mixtures is discussed at nominal and part-load. Finally, the Conclusions section includes the outcomes of the current study and the future perspectives of our work.

METHODOLOGY

In this section, the mGT (2-spool engine) used for the numerical model, is presented. Then, the description of the modeling techniques, that are adopted for this analysis along with the two part-load strategies, are presented.

2-spool intercooled mGT

The basis of this numerical model is a 2-spool mGT which has similar performance characteristics as the Aurelia A400 mGT [12]. This engine is a recuperated Brayton cycle and consists of two shafts as it is shown in Figure 1. The low-pressure compressor (LPC), low-pressure generator and low-pressure turbine (LPT) are mounted on the low-pressure shaft (LPS). Additionally, the high-pressure compressor (HPC), high-pressure generator and high-pressure turbine (HPT) are part of the high-pressure shaft (HPS). The recuperator uses the exhaust gases to increase the enthalpy of the working fluid before it enters the combustion chamber (CC) (5). The other heat exchanger (i.e., the Intercooler) cools down the air at the HPC inlet (3) to increase the component's isentropic efficiency. The electrical power is generated from the two high-speed power generators and the power electronics needed to convert the two produced powers to grid frequency. This cycle can achieve an electrical efficiency higher than 40 % for a nominal power of 400 kW [12]. The typical specifications of this engine are shown in Table 1. The 2-spool machine operates at constant power and behaves similarly to a single-spool variable speed mGT. Such machines allow the operator to keep the turbine inlet temperature (TIT) constant at high levels while reducing the rotational speed to operate at part load, while still maintaining high electrical efficiency. In this specific engine, however, the two shafts can be controlled independently of each other. This allows the turbomachinery components to run at high efficiency
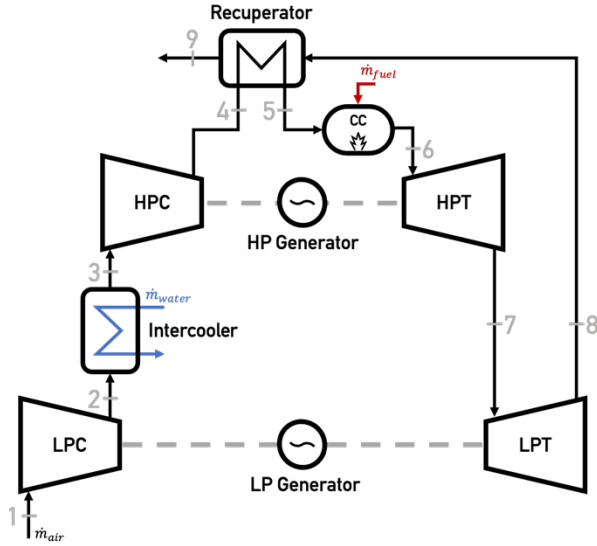
FIGURE 1: The 2-spool mGT is a two-shaft recuperated Brayton cycle with an Intercooler between the low-pressure and high-pressure compressor. The Intercooler decreases the temperature at point 3 to increase the air density and efficiency of the high-pressure compressor. The recuperator preheats the air coming from the compressor with the exhaust hot gases.

for a larger operating range than with a single-shaft engine. Therefore, as the demanded power is decreased, the rotational speeds are decreased and TIT is kept constant by the controller. When the maximum allowable turbine exhaust temperature (TET) is reached at 40% load, the TIT is starting to reduce as well. Then, the electrical efficiency of the engine experiences a sharp decrease, as presented by Jaatinen-Värri et al. [25] with the cooperation of Aurelia Turbines Oy [12].

TABLE 1: The nominal specifications of Aurelia A400 given by the manufacturer [12].

Nominal electric power, $P_{e,nom}$	400 kW$_e$
Nominal electrical efficiency, $\eta_{el,nom}$	40.2 %
Exhaust gas flow at full power	2.2 kg/s
Exhaust gas temperature at full power	185 ºC

Numerical model

In this subsection the developed in-house numerical model, to study the impact of fuel alteration on the performance of a 2-spool mGT is extensively described. This software can predict the nominal and part-load behavior of a 2-spool mGT by using two different part-load schemes.

The modeling methods that are applied to each component of the mGT cycle are similar to a previous study from part of the authors [26]. In this study, the results of the transient T100 mGT were validated in steady-state and transient conditions. For the current study due to the lack of experimental results and data from the manufacturer, our model adopted the design, boundary and initial conditions from the available studies on the
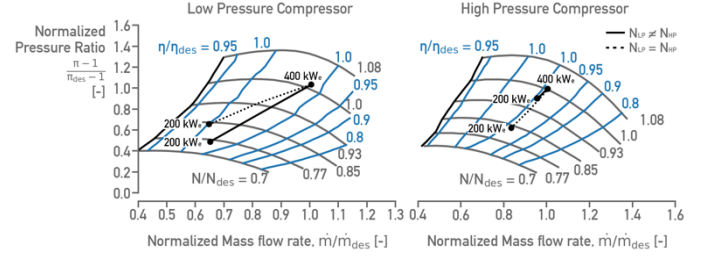
FIGURE 2: Compressor performance maps generated by digitization of the data presented by Jaatinen-Värri et al. [14]. The evolution of the operating point, depending on the control strategy in both maps, is presented.

Aurelia A400. After the description of the modeling methods, the complete model is compared with another study from the literature [13] and with the design specifications of Aurelia A400 [12] to confirm the accurately developed methodology (see later).

The fluid properties are modeled using different equations of state from the Coolprop library [27]. For example, the fluid behavior of water is calculated with IAPWS (International Association for the Properties of Water and Steam) 1995 [28]. The great advantage of this library is the representation of real gas behavior compared to most equations of state that emanate from the assumption of ideal gas behavior using reference states.

The compressor maps are extracted from literature [14] and digitized to calculate the pressure ratio and isentropic efficiency of the LPC and HPC. Figure 2 presents the LPC and HPC maps. The values are normalized using the design (des) parameters of the maps. The design parameters correspond to the compressors' nominal conditions at 400 kW$_e$ and are shown in Table 2. These values were extracted for Malkamäki et al. [13] and are used to calculate the normalized pressure ratio, isentropic efficiency and reduced (red) shaft speeds ($N_{red} = N/\sqrt{T_{in}}$) and mass flow rate ($\dot{m}_{red} = \dot{m}\sqrt{T_{in}}/p_{in}$) from the two compressors. The rotational speeds of the LPS and HPS are equal at nominal conditions so the design shaft speed is 33200 rpm for both compressors. The model applied the same fitting techniques that were presented in a previous study from part of the authors [26] for both compressors using a Supershape fitting equation for the pressure ratio and an Ellipse equation for the efficiency. As a result, the

TABLE 2: The design compressor parameters are calculated from Malkamäki et al. [12] and are the nominal conditions of the two compressors.

Design rotational speed, N_{des}	33200 rpm
Design mass flow rate, $\dot{m}_{air,des}$	2.085 kg/s
Design LPC pressure ratio, $\pi_{LPC,des}$	2.7
Design HPC pressure ratio, $\pi_{HPC,des}$	1.846
Design LPC isentropic efficiency, $\eta_{LPC,des}$	0.8
Design HPC isentropic efficiency, $\eta_{HPC,des}$	0.82
Design LPT, HPT isentropic efficiency, $\eta_{T,des}$	0.84

pressure ratio and the isentropic efficiency are calculated using the mass flow rate and the rotational speed as inputs for each component (LPC, HPC). The outlet enthalpy of the compressor components is calculated using the isentropic efficiency ($\eta_{is,c}$) as in Eq. 1:

$$h_{out} = h_{in} + \frac{h_{out,is} - h_{in}}{\eta_{is,c}} \tag{1}$$

where h_{in} is the specific enthalpy of air at the inlet of each compressor, $h_{out,is}$ is the specific enthalpy at constant specific entropy ($s_{in} = s_{out}$). The outlet temperature is given using the fsolve function from the SciPy library [29]. Therefore, for a given fluid composition and specific enthalpy, this algorithm finds the temperature when $h(T_{out}) - h_{out} = 0$. Moreover, the compressor surge margin which is a useful value to determine whether the component experiences flow instabilities is calculated as presented below (Eq. 2):

$$SM = \left. \frac{\dot{m}_c - \dot{m}_{c,sl}}{\dot{m}_c} \right|_{N=const} \cdot 100\% \tag{2}$$

where $\dot{m}_{c,sl}$ is the mass flow rate of at the surge line considering constant rotational speed.

The HPT is considered choked in the simulations. This assumption is adopted due to the lack of any information regarding the turbine performance maps and it is considered a standard practice in gas turbine modeling. As a result, the maximum amount of mass flow rate through the HPT is fixed by the choking constant which is presented as [30] (Eq. 3):

$$K_c = \frac{\dot{m}_{HPT}\sqrt{TIT}}{p_{in,HPT}} = A\sqrt{\frac{k_{HPT}}{R}\left(\frac{2}{k_{HPT}+1}\right)^{\frac{k_{HPT}+1}{k_{HPT}-1}}} = const \tag{3}$$

where $p_{in,HPT}$ is the pressure at the inlet of the turbine, k_{HPT} is the average heat capacity ratio of the gas at the HPT, R corresponds to the gas constant and A is the cross-sectional area of the turbine. First of all, the cross-sectional area is calculated by running the simulation at nominal conditions and knowing the $\dot{m}_{HPT}, TIT$ and $p_{in,HPT}$. Then this value is used to calculate the choke constant. Introducing different fuel properties in the cycle, the k_{HPT} changes, depending on the heat capacity of the gases in the outlet of CC. The initial isentropic efficiency in both turbines is assumed to have the value that is shown in Table 2. Similarly, the influence of k on the initial isentropic efficiency of the HPT and LPT is addressed for the gas properties change. This is done, as suggested by Parente et al. [31], with Eq. 4.

$$\frac{\eta_{is}}{\eta_{is}^*} = \frac{k-1}{k^*-1}\sqrt{\frac{k^*+1}{k+1}\frac{1-1/\pi^{(k^*-1)/k^*}}{1-1/\pi^{(k-1)/k}}} \tag{4}$$

The apex (*) refers to the properties of standard dry air and π to the pressure ratio of the component. This equation was proposed by Parente et al. [31] for humidified mGTs, but can also be applied for fuel alterations. The HPT pressure ratio is an input and a control variable in this model, while the LPT pressure ratio is calculated by assessing the pressure losses in the recuperator hot side to find p_8 (see Figure 1). The HPT and LPT outlet temperatures are calculated the same way as the outlet temperature of the compressors using fsolve. The outlet specific enthalpy is derived from Eq. 5:

$$h_{out} = h_{in} - \eta_{is,T}(h_{in} - h_{out,is}) \tag{5}$$

Regarding the heat exchanger modeling, a correlation was made for the recuperator effectiveness (ε_{rec}) based on the information from Jaatinen-Värri [25]. Therefore, the effectiveness is a function of the mass flow rate at the cold side inlet (point 4). A constant value was adopted for the intercooler effectiveness (ε_{int}) due to the limited information regarding this component. As a result, the effectiveness is assumed 0.9155 to match the HPC inlet temperature presented by Jaatinen-Värri et al. [14] at nominal conditions. The temperature at the outlet of the intercooler hot side (point 3) and recuperator cold side (point 5) is given with the equations below:

$$T_5 = T_4 + \varepsilon_{rec}(T_8 - T_4) \tag{6}$$
$$T_3 = T_2 - \varepsilon_{int}(T_2 - T_{w,in}) \tag{7}$$

where $T_{w,in}$ is the inlet temperature of the water at the cold side of the intercooler and it is kept at 15 °C during the simulations. The cold side of the intercooler utilizes water with a sufficient mass flow rate of 2.1 kg/s. The numbering of equations (6) and (7) corresponds to the different states shown in Figure 1.

At the CC outlet, the temperature (TIT) is kept constant and equal to 977 °C. This temperature is considered acceptable for the materials of the HPT and corresponds to the information derived from a company associated with Aurelia Turbines [32]. The gas properties after the combustion process are calculated with the object-oriented Cantera software [33] using the GRI-Mech 3.0 library. The code uses the method "equilibrate" that invokes Cantera's chemical equilibrium solver, which uses an element potential method. The element potential method is one of a class of equivalent nonstoichiometric methods that solves a set of N nonlinear algebraic equations, where N is the number of elements (not species). The gas properties are determined by knowing the fuel-to-air ratio (FAR), the TIT and the thermodynamic properties at point 5 (Figure 1). Therefore, an initial value for the FAR is assumed and the new FAR is determined by solving the energy balance (Eq. 8) of CC with an iterative method.

$$FAR_{new} = \frac{(FAR + 1)h_6 - h_5}{LHV \cdot \eta_{cc}} \tag{8}$$

5

η_{cc} corresponds to the combustion efficiency of CC and is 0.99. Also, the pressure losses at CC are taken into account as equal to 3%.

The power ratio (P_eR) between the generated power of HPS and LPS is extracted from the literature and has a value of 1.1473 [25]. This power ratio is considered when the LPS and HPS have the same rotational speed at nominal load. The two generators have 96% electromechanical efficiency and the efficiency of the inverter is 98%.

The complete steady-state model of the cycle operating with dry air is presented in Figure 3. The model uses an iterative method that starts at the inlet of the cold side of the recuperator to accurately calculate the inlet hot side temperature T_8. We assume a value of T_8 to calculate the T_5 in the recuperator block and then determine the thermodynamic values in the inlet and outlet of CC and Turbine blocks until the error of T_8 between iterations is below 10^{-5}. The external iteration essentially controls the mGT cycle. The simulation converges by changing three user-defined constant values using the Secant method.
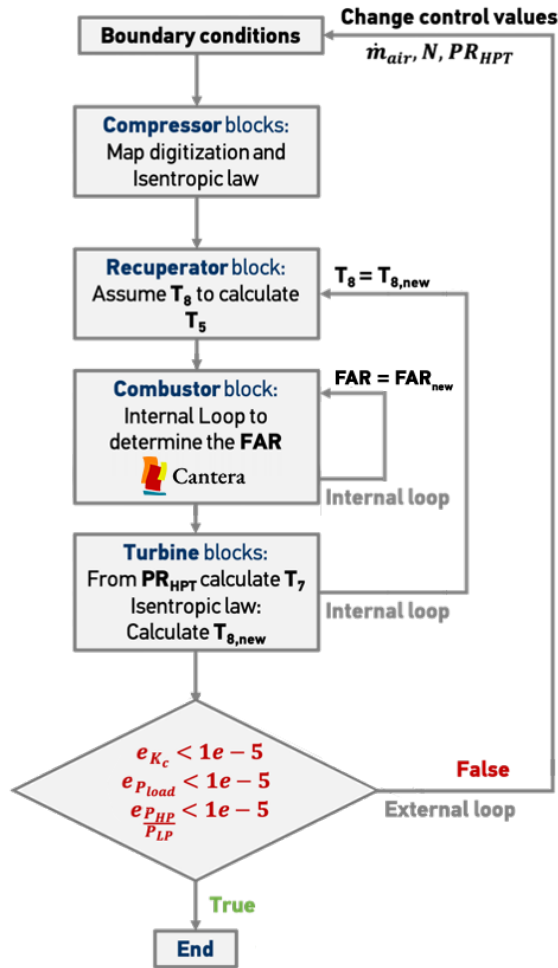
FIGURE 3: Flow chart of the calculation steps of the 2-spool mGT 0-D model. Three control parameters are used to keep the choke constant, electric power and power ratio at specific values.

Therefore, $\dot{m}_{air}$ controls K_c, $N = N_{LP} = N_{HP}$ controls the electrical power (P_e) and PR_{HPT} controls $P_eR = P_{HP}/P_{LP}$.

Part-load management

Two different part load control schemes are employed. The first scenario (case 1) considers the LPS and HPS to run at equal rotational speeds. This control scheme allows us to use only the N_{LP} as a value that adjusts the produced electric power. As a result, the unknown parameters of the system are only the 3 control variables that enable the model to converge. In the second scenario (case 2), N_{LP} and N_{HP} operate at different rotational speeds. The LPS rotational speed is the control value that determines the produced power like case 1, but the HPS rotational speed is a function of the electric power according to Eq. 9:

$$N_{HP} = f(P_e) \cdot N_{LP} \qquad (9)$$

The correlation between the generated power and the HPS rotational speed is derived from a study on the control strategies of Aurelia A400 [25]. Also, the power ratio (P_eR) should be a function of the produced electric power ($P_eR = f(P_e)/P_{e,nom}$) as the two shafts are not loaded equally. Both correlations are made with a linear interpolation between the input values. Thus, by applying these two correlations to case 2, it is possible to utilize the part-load control scheme that is suggested by the Aurelia A400 studies in the literature [14,25]. Figure 2 shows the operating lines of case 1 ($N_{LP} = N_{HP}$, dashed line) and case 2 ($N_{LP} \neq N_{HP}$, solid line) in both high-pressure and low-pressure compressor maps. The LPC operating line of case 2 is observed in the high-efficiency region as shown in Figure 2. Whereas in case 1, the reduction in pressure ratio at part-load is less, compared to the nominal point. Also, case 1 presents lower efficiencies for the same mass flow rate. The HPC operating line of case 2 shows higher pressure ratios than case 1 to compensate for the behavior of the LPC operating line. As a result, case 2
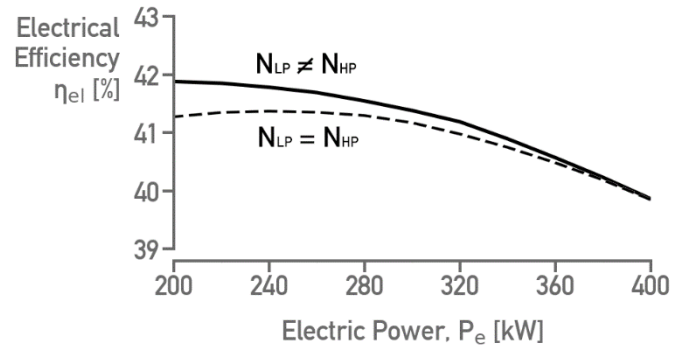
FIGURE 4: Electrical efficiency behavior from 200 to 400 kW versus the produced electric power at two different control schemes (case 1: $N_{LP} = N_{HP}$, case 2: $N_{LP} \neq N_{HP}$). The two part-load management methods do not show significant divergence in efficiency. At half the nominal load, case 2 presents higher efficiency of less than absolute 1% than case 1.

HPC operates in a small pressure ratio and shaft speed region compared to case 1.

Figure 4 depicts the electrical efficiency behavior at part load until 200 kW$_e$ in both cases. As it is shown case 2 presents slightly higher efficiency on the whole operating range. However, the efficiency difference is rather small and less than 1% even in 50% of the nominal load. Moreover, the efficiency increases as the generated electric power drops. On the other hand, in case 1, the efficiency starts to drop after 280 kW. Also, no significant difference in efficiencies is observed from 400 to 350 kW.

Model comparison

The developed 0-D model is compared to a model presented in literature about the Aurelia A400 prototype [14]. For this comparison, the model should operate with the same parameters that have been described above (Table 1,2) except for the TIT and $T_{w,in}$ to match the operating conditions of the study [14]. Therefore, the TIT is kept at 1077 °C, $T_{w,in}$= 5 °C and the produced power is set at 455 kW$_e$, as this was the power reported on the specific work of the prototype. However, this power output is only used for the comparison of the two models. After the verification of our model, we will use the characteristics of the commercialized version, meaning that we limit our analysis to 400 kW$_e$. Figure 5 presents the relative error of temperature and pressure at points 2,3,4,5,7,8 (see Figure 1). The relative error is calculated with the following expression (Eq. 10):

$$e = \frac{|x_p - x|}{x_p} 100\%. \qquad (10)$$

The values of our model are shown as x and the values of the study [14] as x_p.

The values of temperature and pressure present an error below 0.7 % which confirms the accurate use of the component
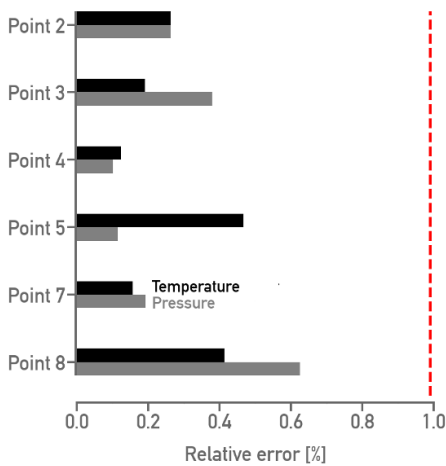
FIGURE 5: Relative error for the steady-state comparison of our model and the model of Jaatinen-Värri et al. [14] at operating load of 455 kW$_e$. The error is below 0.7% for the values of pressure and temperature.

methods that were applied for this study (Figure 5). Also, the relative error of the electrical efficiency is 5.96 %, as the electrical efficiency of the study [14] and the one we calculated are 45.8 % and 43.07 % accordingly. The increased error of the electrical efficiency could be associated with the fact that our simulation model does not use the turbine performance maps to calculate the operating parameters (pressure ratio and shaft speed) of HPT and LPT. Moreover, the study [14] has no information regarding the LHV of natural gas in this publication.

The part-load performance of the model is compared with the only available data regarding the Aurelia A400 in the literature. Therefore, the partial load efficiency of this machine was extracted with digitization from the Aurelia Turbines Oy datasheet [12]. This data is depicted with a blue line in Figure 6. In this part-load comparison, the model runs with a TIT of 977 °C and $T_{w,in}$= 5 °C as suggested by [32] in each produced power that is set. As a result, the operating conditions of this comparison differ from the comparison that is conducted in Figure 5. The results of Figure 6 show that the efficiency relative error between the Aurelia Turbines Oy datasheet and the model is below 0.75 %. The highest error is 0.742 % and is observed at 200 kW$_e$. Also, the results of the model follow adequately the efficiency data and have a similar trend. Thus, both comparisons confirm the accuracy of our modeling methods and allowed us to utilize this code to carry out a performance assessment in the current study.
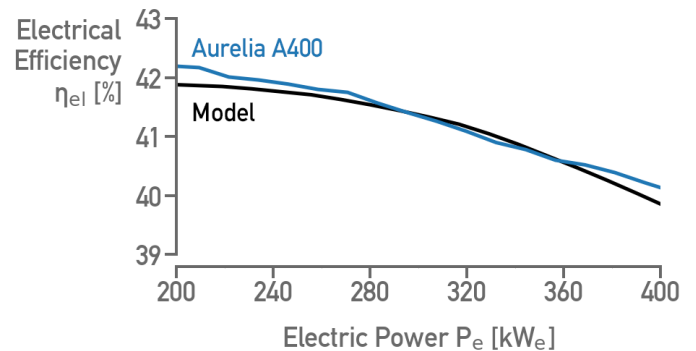
FIGURE 6: Steady-state results of electrical efficiency (black line) at an electric power range of 200-400 kWe compared with the electrical efficiency presented from Aurelia Turbines Oy datasheet [12] (blue line). The part-load relative error does not exceed 0.75 % which is sufficient.

Fuel consideration

In this subsection, the fuels that are used for this analysis are described. Firstly, the compositions of syngas should be chosen with care as the volume percentage of hydrogen (H$_2$) and carbon monoxide (CO) influence dramatically the LHV of the fuel and the combustion characteristics in general.

Syngas (SG) can be produced in several ways, while the hydrogen percentages vary depending on the quality of the fuel input. Wood chips should have a moisture content of 20% to produce the maximum amount of hydrogen and lower tar. The presence of hydrogen in syngas generated by wood ranges

between 5% and 30% based on literature data [34–37]. For the current study, we considered an average amount of moisture in the wood chips. As a result, the amount of H_2 is 15.46% as shown in Table 3. Moreover, natural gas (NG) is composed mainly of methane with a percentage of 91.2% with the ethane and propane amount to be lower than 10%. Table 3 shows that the LHV of syngas is 47% of the LHV of natural gas. This difference in the stored energy of these two fuels could significantly alter the engine's operating conditions. The third fuel that we use for the testing of different mixtures in the 2-spool mGT cycle is pure hydrogen with 119.90 MJ/kg lower heating value.

TABLE 3: Natural gas (NG), syngas (SG) compositions and LHV.

	Compositions [vol. %]							LHV [MJ/kg]
	CH_4	C_2H_6	C_3H_8	CO	CO_2	N_2	H_2	
NG	91.2	6.7	2.1	-	-	-	-	49.78
SG	3.05	-	-	31.46	5.03	45	15.46	23.41
H_2	-	-	-	-	-	-	100	119.90

RESULTS AND DISCUSSION

In this section, the numerical results of the model using different fuel mixtures composed of natural gas (NG), syngas (SG) and hydrogen (H_2) are presented. The steady-state model applied two different control schemes for the part load operation and the results are depicted as well. In the control scheme of case 1, the rotational speeds of LPS and HPS have the same value at part-load. Whereas, in case 2 the shaft speeds are not equal except for the nominal conditions. Thus, the solid-line curves, in the figures below, refer to simulations performed using the control scheme of case 2 ($N_{LP} \neq N_{HP}$) and the dashed lines belong to case 1 ($N_{LP} = N_{HP}$).

For the first step of the analysis, we increased the amount of hydrogen and syngas in a blend with natural gas at three different operating points. So, the electrical efficiency, at a generated electric power of 400, 300 and 200 kW, is calculated by varying the syngas and hydrogen content of the fuel from 0 vol.% to 100 vol.% with 10 vol.% increments. Secondly, we present the behavior of different fuel mixtures of syngas and hydrogen at a generated power range of 200 to 400 kW with a power step of 10 kW. The electrical efficiency is calculated as (Eq. 11):

$$\eta_{el} = \frac{P_e}{\dot{m}_f LHV} \qquad (11)$$

$\dot{m}_f$ is the fuel flow rate that is injected in the cycle.

Fuel variation at constant power

As the volume percentage of hydrogen is increased in natural gas from 0% to 100%, the LHV of the fuel mixture increases significantly. This will lead to a decrease in the fuel flow rate. With pure natural gas as baseload, the fuel flow rate is 20.2 g/s and with pure hydrogen 8.34 g/s. This results in a

58.2 % fuel flow decrease. Due to the increased water content of the flue gases, the density and specific heat capacity at point 6 increase. This change in heat capacity of 1.32 % leads to a slight drop in the air mass flow rate of 1.41 %. All these minor changes, in the conditions of the engine at pure hydrogen, move the operating point of the LPC and HPC in the performance map approximately 0.1 % towards the surge limit. This divergence in the operating conditions is very small and the change of electrical efficiency is below 0.2 % not only at nominal but also at part load for both control schemes (case 1 and case 2).

Although we do not see any significant performance alteration when we increase the amount of hydrogen in the fuel, syngas presents a major impact. The amount of syngas in natural gas is increased from 0 to 100 vol. % at 200, 300 and 400 kW of electric load with a 10 vol.% step. The results of electrical efficiency are shown in Figure 7. We observe that at nominal load (black line) the performance of the cycle remains somewhat constant around 39.88 %. Only from 90 to 100 vol.%, the efficiency is slightly decreased. When applying the operational strategy of case 1 ($N_{LP} = N_{HP}$, dashed lines) at part-load, the efficiency at pure natural gas on 300 and 200 kW is almost identical at 41.2 % (dashed lines at 0 vol.% SG content) which is also confirmed by Figure 4. In Figure 4 we can see that from
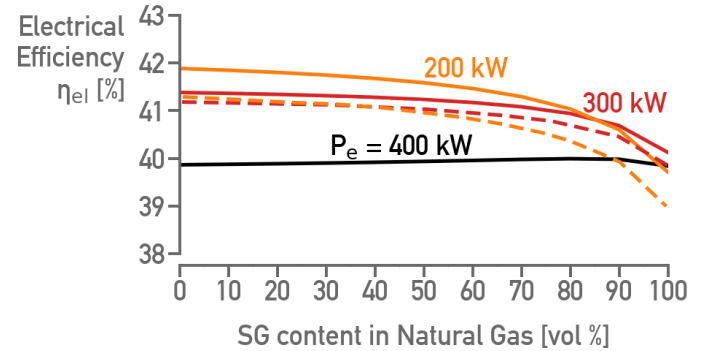
FIGURE 7: Electrical efficiency behavior as the volume percentage of syngas increases at two part-load operational schemes (case 1: dashed line, case 2: solid line). The full load performance does not present significant change. 50-100 % of syngas decreases the efficiency by 2% at 200 and 300 kW in both cases 1 and 2.

310 to 200 kW the efficiency line of case 1 flattens. The performance of case 1 starts to decrease dramatically when the syngas volume percentage exceeds 50% in natural gas (Figure 7). The efficiency at 300 kW shows 1.3 % and at 200 kW 2.31 % absolute decrease at 100 % syngas. Case 2 ($N_{LP} \neq N_{HP}$, solid lines) presents a higher efficiency at the two part-loads with a variable syngas fraction than case 1. At 300 kW the efficiency of pure syngas even shows an absolute increase of 0.28% and at 200 kW of 0.94 %. Furthermore, the efficiency of case 2 does not increase dramatically as we decrease the load in the range of 70-100 % of syngas in the fuel mixture. Thus, at high amounts of syngas, the efficiency remains rather constant as the power drops. At the range of 0-70 % of syngas, the efficiency increases monotonously as the electric power decreases.
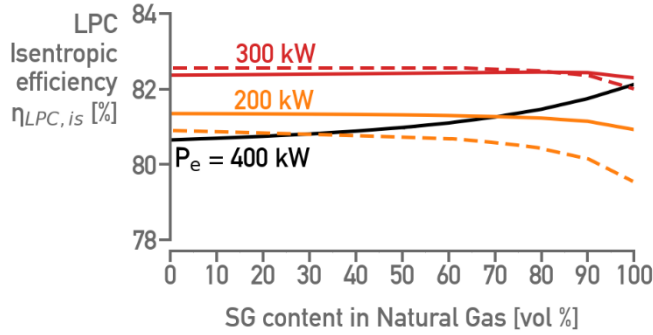
FIGURE 8: Isentropic efficiency of LPC at 400, 300 and 200 kW of electric power as the volume percentage of syngas increases in a natural gas - syngas mixture. The efficiency at 200 kW decreases more than 0.3 % in case 1 compared to case 2 in the NG-SG mixture.

The behavior of the part-load efficiency in cases 1 and 2 is associated with the operating conditions of the LPC. Figure 8 depicts the isentropic efficiency of the LPC ($\eta_{LPC,is}$) of the two cases while we increase the volume percentage of syngas into the fuel. At full load (400 kW) the isentropic efficiency of the component increases as we inject more syngas. This assists the electrical efficiency of the cycle to remain constant (see Figure 7). The efficiency at 300 kW does not change significantly in both cases and remains almost constant even at high amounts of syngas which is in line with the behavior of electrical efficiency at 300 kW in Figure 7. At 200 kW the superiority of case 2 is obvious as the isentropic efficiency remains around 83.4 % and enhances the total electrical efficiency of the cycle.

At this part of the analysis, it is necessary to also present the LPC map (not only efficiency, as presented before) to get a full picture regarding the behavior of the 2-spool mGT when syngas as fuel is used. Figure 9 presents the LPC performance map in normalized values. We can observe that by increasing the volume percentage of syngas, the normalized reduced mass flow rate moves towards the surge line in both control strategies. This can be explained by the difference in fuel LHV. As the LHV of the fuel mixture drops in the syngas case, the demanded fuel flow rate in the CC, to reach the required TIT, increases. However, the flue gas mass flow rate is constant as the LPT is choked. This results in a decrease of the air flow rate of both compressors. In case 2 (solid operating lines) the points of pressure ratio and mass flow rate remain in the region of $\eta_{is}/\eta_{is,des} = 1$ while the dashed lines of case 1 operate at higher pressure ratios. This higher-pressure ratio of the line at 200 kW of case 1 decreases the isentropic efficiency of the component as is depicted also in Figure 8.

This significant decrease in air flow rate at pure syngas, which is presented in Figure 9, is linked to a large amount of nitrogen in the fuel (see Table 3). Almost half of the fuel volume is taken by nitrogen which does not take part in the combustion process that gives energy to the flow. As a result, a higher fuel flow rate is needed for the combustion to reach the demanded TIT. This increased fuel flow rate decreases the air flow rate due to the choking condition on LPT. Thus, the additional normalized
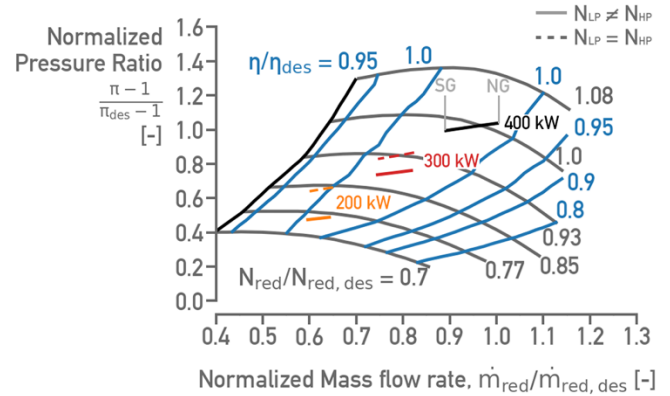
FIGURE 9: The behavior of increasing the syngas content in a natural gas – syngas fuel mixture at 3 electric loads (400, 300, 200 kW) depicted in the low-pressure compressor map. The control strategy of case 1 shows higher pressure ratios and lower isentropic efficiencies compared to case 2.

airflow rate decrease is 7.3 %. Also, the two part-load strategies do not present any significant conclusions on the HPC component. The HPC map presents the operating lines from cases 1 and 2 to be located in the high isentropic efficiency region. Thus, as the HPC isentropic efficiency and also the surge margin remain rather constant, the performance results of HPC in its performance map are not depicted.

As the control scheme of case 1 lets the LPC to operate at higher pressure ratios compared to case 2, it is important to calculate from Eq. 2 and evaluate the surge margin behavior in a natural gas – syngas mixture. Figure 10 shows the surge margin (SM), which is calculated from Eq. 2, in the 3 different generated electric powers. We can see that the SM decreases by 4 % from 60 to 100 vol.% of syngas at full-load. However, SM remains over 25 % even at 200 kW of case 2 which keeps the LPC at a safe operating region even with high-nitrogen syngas fuel. Although, as the load decreases, case 1 moves the operating points more closely to the surge line. Pure syngas fuel has a surge margin of 22.2 % at 300 kW which is considered sufficient, however, at 200 kW the SM goes below 20 % with 70 vol.% of syngas. Moreover, at pure syngas, the SM value at 200 kW load is 17 %. If the nitrogen amount in syngas increases even more,
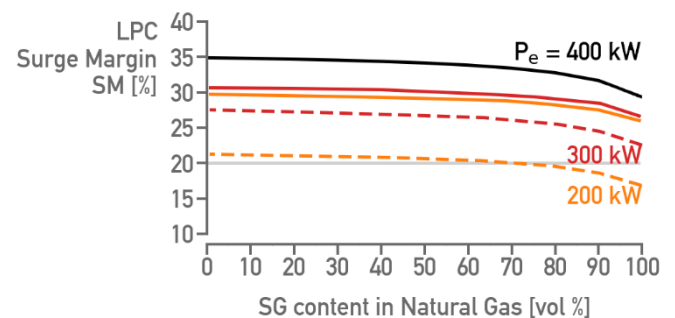

FIGURE 10: Low-pressure compressor surge margin at different mixtures of natural gas – syngas. Case 1 (dashed-line) at 200 kW of electric power shows a surge margin below 20 % which can lead to operational instabilities.

the safe operation of the mGT is not ensured. We should also consider that the utilized performance maps are obtained using digitization and curve fitting methods. As a result, the current modeling uncertainties lead us to consider that case 1 is not a safe operating strategy at loads below 50 % of nominal with pure syngas.

Power variation at constant fuel composition

In this subsection, different fuel mixtures of natural gas, syngas and hydrogen are tested regarding their performance behavior at different loads. Figure 11 presents the electrical efficiency of five different fuel mixtures at an operating range of 200 kW, adopting part-load control strategy case 2. As we discussed in the first paragraph of this chapter, the efficiency curves of pure natural gas (black line) and pure hydrogen (blue line) are very similar and show the highest electrical efficiency. Only below 280 kW, the two lines start to diverge with slightly higher efficiency for NG. However, the difference remains below 0.2 %.

Using syngas lowers the efficiency compared to pure natural gas fuel. One way to compensate, for the lower performance observed with syngas, is the addition of hydrogen to the mixture. As the amount of hydrogen, in a syngas–hydrogen mixture increases (lines red, orange and brown), the efficiency improves and the maximum value moves toward 200 kW. Furthermore, a 15 vol.% hydrogen addition in the fuel (orange line), increases the efficiency at 200 kW of 0.46 %. Also, at 30 % of hydrogen (brown line) the efficiency presents almost a constant behavior at the power range of 240 to 320 kW. Therefore, even a 30 vol.% hydrogen addition counteracts the performance disadvantages of syngas consisting of high nitrogen vol.%. This is logical considering the significantly higher LHV of hydrogen compared to syngas.
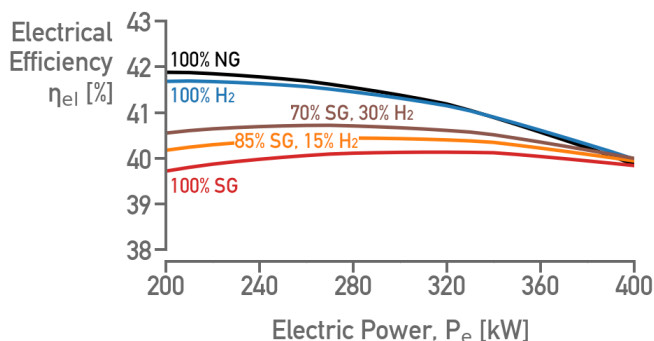
FIGURE 11: Electrical efficiency versus electric power of five different fuel mixtures using control strategy case 2. As the hydrogen content in syngas increases (lines: red 0% SG, orange: 15 % SG and brown: 30 % SG) the efficiency curve becomes flatter at part-load and the maximum performance moves towards lower loads.

CONCLUSIONS

In this paper, a 0-D steady-state model predicted the performance behavior of a 2-spool mGT with alternative fuels by applying two different part-load strategies. The model was developed in Python programming language adopting Cantera object-oriented library to calculate the combustion process effectively. Two different control schemes for the calculation of the part-load operating conditions of the engine are adopted. The first control strategy used shaft speeds with identical rotational speeds (case 1). The second strategy was taken from the literature as it is considered to be one of the most efficient for the 2-spool mGT (case 2). In that strategy, the rotational speed of the LPS controls the produced power and the shaft speed of the HPS is a function of this generated power using a correlation from the literature. Moreover, the model is compared with another study about a 2-spool mGT; temperature and pressure results showed an error below 0.7 %.

Three different fuels are utilized for this performance assessment. We observed the part-load behavior of the mGT for different fuels, natural gas, syngas and hydrogen in the two part-load scenarios (cases 1 and 2). As we add hydrogen to natural gas, the divergence in the operating conditions is insignificant. On the other hand, including syngas in natural gas leads to lower efficiencies. A mixture of natural gas and syngas decreases the air flow rate of the cycle. Pure syngas presents a 7.1 % decrease in normalized air flow rate. The nitrogen content mostly influences the air flow rate decrease in LPC towards the surge line. For this reason, hydrogen could be injected into syngas to counteract the efficiency and surge margin decrease. The superiority of control strategy case 2 is highlighted as it presented increased efficiencies at part-load for 5 different fuel mixtures. Also, the control scheme case 1 showed a surge margin below 20 % when the amount of syngas is over 70 vol.% in natural gas at 200 kW. This indicates that the LPC could present instabilities in its operation for lower loads and higher nitrogen contents in syngas.

The results show the potential of applying alternative fuels with an effective operational strategy. However, in future work, specific attention should be paid to the calculation of the flame speed of the different fuel mixtures using CFD analysis and chemical kinetics software to determine the occurrence of flashback. Furthermore, a fuel dilution method by injecting water or nitrogen into the fuel, to avoid this phenomenon, could be applied.

REFERENCES

[1] Magistri L., Costamagna P., Massardo A.F., Rodgers C., McDonald C.F., A Hybrid System Based on a Personal Turbine (5 kW) and a Solid Oxide Fuel Cell Stack: A Flexible and High Efficiency Energy Concept for the

Distributed Power Market, Journal of Engineering for Gas Turbines and Power, 124 (2002) 850-857

[2] Ferrari, M., L., Traverso, A., Massardo, A., F., 2016, "Smart Polygeneration Grids: Experimental Performance Curves of Different Prime Movers, Applied Energy, Volume 162, Pages 622-630.

[3] Breuhaus, P., Madib, H., Mansouria, M., & Kennedy-Georgec, E. (2021). An Integrated Energy System to Decarbonise Islands–Gas Turbine Roles and Requirements, 10th International Gas Turbine Conference Gas turbines in a carbon-neutral society, Paper ID Number: 61-IGTC21, virtual.

[4] Kolanowski, B. F., 2004, Guide to Microturbines, Fairmont Press, Lilburn, GA; New York.

[5] Boukhanouf, R., 2011, "Small Combined Heat and Power (CHP) Systems for Commercial Buildings and Institutions" Woodhead Publishing, Pages 365-394,

[6] Prasad, K., Jukka, R., 2013, "Generation of Heat and Power from Biogas for Stationary Applications: Boilers, Gas Engines and Turbines, Combined Heat and Power (CHP) Plants and Fuel Cells" The Biogas Handbook, Woodhead Publishing, Pages 404-427,

[7] Pilavachi PA. Mini- and micro-turbines for combined heat and power. J Appl Therm Eng 2002;22:2003–14.

[8] Al Moussawi, H., Fardoun, F., Louahlia-Gualous, H., 2017, "Selection based on differences between cogeneration and trigeneration in various prime mover technologies", Renew Sustain Energy Rev, Vol. 74 (2017), pp. 491-511.

[9] Javanshir, A., Sarunac, N., Razzaghpanah, Z., 2017, "Thermodynamic Analysis of ORC and Its Application for Waste Heat Recovery", Sustainability, Vol. 9 issue 11, pp.1974.

[10] De Paepe, W., Carrero, M. M., Bram, S., Parente, A., and Contino, F., 2014, "Experimental Characterization of a T100 Micro Gas Turbine Converted to Full Humid Air Operation," Energy Procedia, 61, pp. 2083–2088.

[11] Tiwari, R., N., Reggio, F., Renuke, A., Pascenti, M., Traverso, A., Ferrari, M.L., 2022, "Performance Investigation of a Bladeless Air Compressor" *J. Eng. Gas Turbines Power*, Vol-144(9)

[12] Aurelia Turbines Oy, (2018), https://aureliaturbines.com/

[13] Malkamäki, M., Jaatinen-Värri, A., Honkatukia, A., Backman, J., & Larjola, J., 2015, "A High Efficiency Microturbine Concept" 11th European Conference on Turbomachinery Fluid dynamics & Thermodynamics ETC11, March 23-27, 2015, Madrid, Spain.

[14] Jaatinen-Värri, A., Nerg, J., Uusitalo, A., Ghalamchi, B., Uzhegov, N., Smirnov, A., Malkamäki, M., 2016., "Design of a 400 kW Gas Turbine Prototype. ASME Turbo Expo: 2016: Power for Land, Sea, and Air Paper No: GT2016-56444, (Vol. 49866, p. V008T23A007).

[15] Mansouri, M., Madi, H., & Breuhaus, P., 2022, "Establishment of a Baseline Integrated Energy System to Decarbonise Geographical Islands". In Turbo Expo: Power for Land, Sea, and Air, Paper Number: GT2022-82918.

[16] Shih, H.-Y., Liu, C.-R. A computational study on the combustion of hydrogen/methane blended fuels for a micro gas turbines. Int. J. Hydrogen Energy 2014, 39, 15103–15115.

[17] Rajpara, P., Shah, R., Banerjee, J. 2018, "Effect of Hydrogen Addition on Combustion and Emission Characteristics of Methane Fuelled Upward Swirl can Combustor". Int. J. Hydrogen Energy 2018, 43, 17505–17519.

[18] Cappelletti, A., Martelli, F., 2017 "Investigation of a pure hydrogen fueled gas turbine burner." Int. J. Hydrogen Energy 2017, 42, 10513–10523.

[19] Pappa, A., Bricteux, L., Bénard, P., and De Paepe, W. "Can Water Dilution Avoid Flashback on a Hydrogen-Enriched Micro-Gas Turbine Combustion—A Large Eddy Simulations Study." ASME. J. Eng. Gas Turbines Power. April 2021; 143(4): 041008.

[20] Bompas, J., De Paepe, W. (2021). Fuel Flexibility of a 100kWe Micro Gas Turbine: Combustion Performance Using Natural Gas and Non-Conventional Syngas, International Conference on Applied Energy 2021 Nov. 29 - Dec. 5, 2021, Thailand/Virtual Paper ID: 487

[21] Diaz, R., Ochoa, G. V., & Peralta, Y. 2018, "Exergoeconomic Analysis of a Syngas Micro Turbine Cogeneration System", Chemical Engineering Transactions, 65, 655-660.

[22] Reale, F, Sannino, R, Calabria, R, & Massoli, P. "Numerical Study of a Small-Scale Micro Gas Turbine-ORC Power Plant Integrated With a Biomass Gasifier." Proceedings of the ASME Turbo Expo 2020: Turbomachinery Technical Conference and Exposition. Volume 8: Industrial and Cogeneration; Manufacturing Materials and Metallurgy; Marine; Microturbines, Turbochargers, and Small Turbomachines. Virtual, Online. September 21–25, 2020. V008T20A020. ASME.

[23] Renzi, M., Patuzzi, F., and Baratieri, M., 2017. "Syngas feed of micro gas turbines with steam injection: Effects on performance, combustion and pollutants formation". Applied Energy, 206, pp. 697 – 707.

[24] De Paepe, W., Renzi, M., Carrerro, M. M., Caligiuri, C., and Contino, F. (September 26, 2018). "Micro Gas Turbine Cycle Humidification for Increased Flexibility: Numerical and Experimental Validation of Different Steam Injection Models." ASME. J. Eng. Gas Turbines Power. February 2019; 141(2): 021009.

[25] Jaatinen-Värri, A, Backman, J, Honkatukia, J, & Malkamäki, M. "A Comparison of Small-Scale Gas Turbine Control Schemes." Proceedings of the ASME Turbo Expo 2017: Turbomachinery Technical Conference and Exposition. Volume 8: Microturbines, Turbochargers and Small Turbomachines; Steam Turbines. Charlotte, North Carolina, USA. June 26–30, 2017. V008T26A020. ASME.

[26] Gaitanis, A., Contino, F., and De Paepe, W. "Real Time MGT Performance Assessment Tool: Comprehensive

Transient Behaviour Prediction with Computationally Effective Techniques." ASME. J. Eng. Gas Turbines Power.

[27] Bell, I. H., Wronski, J., Quoilin, S., and Lemort, V., 2014. "Pure and pseudo-pure fluid thermophysical property evaluation and the open-source thermophysical property library coolprop". Industrial & Engineering Chemistry Research, 53(6), pp. 2498–2508.

[28] Wagner, W.; Pruß, A. The IAPWS formulation 1995 for the thermodynamic properties of ordinary water substance for general and scientific use. J. Phys. Chem. Ref. Data 2002, 31, 387–535.

[29] Virtanen, P., Gommers, R., Oliphant, T.E. et al. SciPy 1.0: fundamental algorithms for scientific computing in Python. Nat Methods 17, 261–272 (2020).

[30] Yanus A. Cengel and Michael A. Boles. Thermodynamics: an engineering approach. ISBN 007-125084-0. McGraw Hill, 2006.

[31] Parente, J., Traverso, A., and Massardo, A.. Micro Humid Air Cycle: Part A – Thermodynamic and technical aspects. In Proceedings of ASME Turbo Expo 2003, number GT2003-38326, pages 221–229, 2003.

[32] Endowers Solutions Pvt. Ltd, (2021), https://www.endowers.in/

[33] David G. Goodwin, Harry K. Moffat, Ingmar Schoegl, Raymond L. Speth, and Bryan W. Weber. Cantera: An object-oriented software toolkit for chemical kinetics, thermodynamics, and transport processes. https://www.cantera.org, 2022. Version 2.6.0.

[34] Montagnaro, F., & Zaccariello, L., 2022, "Gasification of Spruce Wood Chips in a 1.5 MWth Fluidised Bed Reactor", Energies, 15(16), 5883.

[35] El-Nagar, R. A., & Ghanem, A. A., 2019, "Syngas production, properties, and its importance" (Vol. 2, pp. 1-8). London, UK: Intech Open.

[36] Bandara, J.C.; Jaiswal, R.; Nielsen, H.K.; Moldestad, B.M.E.; Eikeland, M.S., 2021 "Air gasification of wood chips, wood pellets and grass pellets in a bubbling fluidized bed reactor", Energy 2021, 233, 121149.

[37] Lalsare, A., Wang, Y., Li, Q., Sivri, A., Vukmanovich, R. J., Dumitrescu, C. E., & Hu, J., 2019, "Hydrogen-rich syngas production through synergistic methane-activated catalytic biomass gasification", ACS Sustainable Chemistry & Engineering, 7(19),16060–16071.